Sustainable Energy, Grids and Networks 43 (2025) 101814

Contents lists available at ScienceDirect

Sustainable Energy, Grids and Networks

journal homepage: www.elsevier.com/locate/segan

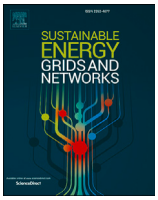

Modeling and optimal operation of sustainable thermoelectric microgrids with phase-change material thermal system

Pablo Verdugo [a], Claudio Cañizares [a,*], Mehrdad Pirnia [a], Thomas Leibfried [b]

[a] Dept. of Electrical Computer Engineering, University of Waterloo, Waterloo, Canada
[b] Inst. of Electric Energy Systems High-Voltage Technology, Karlsruhe Institute of Technology, Karlsruhe, Germany

ARTICLE INFO

keywords:
Building thermal modeling
Energy management system
Energy smart home lab
Thermoelectric microgrid
Phase-change material

ABSTRACT

This paper proposes an Energy Management System for a thermoelectric microgrid that incorporates the modeling of a unique Phase-Change Material-based thermal system, capable of operating in both active and passive modes to minimize operating costs while guaranteeing thermal comfort, while properly considering the microgrid's thermal power requirements and indoor temperature control. The proposed model also includes a detailed thermal representation of buildings to consider relevant thermal sources and room heat exchange, as well as heat pumps, water tanks for thermal storage, and battery degradation. A Model Predictive Control approach is used to address uncertainties in demand and environmental conditions. The proposed Energy Management System model is applied to the Energy Smart Home Lab microgrid located at the Karlsruhe Institute of Technology, in Germany, taking into account the specific characteristics of the microgrid's components, expected energy consumption, and indoor temperature control requirements. Simulation results demonstrate the feasible application of the developed Energy Management System for the optimal operation of the actual microgrid considered, illustrating the thermoelectric microgrid's power balance and temperature fluctuations of the associated components, with particular emphasis on the operation of the Phase-Change Material system, to showcase its active and passive thermal contribution under extreme weather conditions.

1. Introduction

Achieving net zero in the building sector demands a substantial increase in the provision of electricity through sustainable resources that also consider space heating and cooling. However, balancing the affordability and reliability of such resources while managing peak demand presents a considerable challenge for electric utilities and customers. In recent years, many initiatives addressing climate change and supporting the transition to a low-carbon economy have proposed the use of Microgrids (MGs) to facilitate the integration of clean energy generation sources and the electrification of thermal energy systems to achieve CO2 Net Zero goals.

MGs are clusters of controllable and uncontrollable loads and Distributed Energy Resources (DERs), comprising Distributed Generation (DG), Energy Storage Systems (ESSs), Renewable Energy Sources (RESs), and Demand Response (DR) operated in coordination to reliably supply electricity [1], while also considering thermal power requirements [2–4]. The Energy Management System (EMS) of thermoelectric (TE) MGs must be capable of controlling both electric and thermal resources to ensure a reliable and cost-effective operation while satisfying customers' needs [2]. Thus, securing the optimal operation of such MGs is a challenging task, requiring the modeling of the energy resources such as RESs and Battery Energy Storage Systems (BESSs), while accounting for the variability of energy demand and environmental conditions, as well as other components such as heating/cooling systems and users' thermal comfort through proper temperature settings, which add to the complexity of the model.

Much research has been dedicated to the study of these TE-MGs, with some researchers considering the thermal demand as an input parameter to the EMS [5–11], and others incorporating building thermal modeling to account for indoor temperature control, considering the building as a single space [2–4,12–16]. Few authors have addressed the incorporation of models that allow detailed representation of different rooms in a building, particularly in the context of MGs and multiple TE resources. For example, in [17], a Price Storage Control

* Corresponding author.
Email addresses: pverdugo@uwaterloo.ca (P. Verdugo), ccanizar@uwaterloo.ca (C. Cañizares), mpirnia@uwaterloo.ca (M. Pirnia), thomas.leibfried@kit.edu (T. Leibfried).

https://doi.org/10.1016/j.segan.2025.101814
Received 26 November 2024; Received in revised form 28 March 2025; Accepted 23 July 2025
Available online 26 July 2025

Nomenclature

Acronyms

AC	Air Conditioner
BESS	Battery Energy Storage System
CHP	Combined Heat and Power
COP	Coefficient of Performance
DER	Distributed Energy Resource
DG	Distributed Generation
DOD	Depth of Discharge
DR	Demand Response
EMS	Energy Management System
ESHL	Energy Smart Home Lab
ESS	Energy Storage System
EV	Electric Vehicle
GHG	Green-House Gas
HP	Heat Pump
HVAC	Heating Ventilation and Air Conditioning
KIT	Karlsruhe Institute of Technology
MG	Microgrid
MPC	Model Predictive Control
PCM	Phase-Change Material
PV	Photo-Voltaic
RES	Renewable Energy Source
SOC	State of Charge
TE	Thermoelectric
TEC	Thermal Equivalent Circuit
TES	Thermal Energy Storage
TOU	Time-of-Use

Sets and Indices

$\underline{\cdot}, \overline{\cdot}$	Minimum and maximum limits
$\{LA\}$	Living area
$\{TR\}$	Technical room
$f \in F$	Floors of building
$i, j \in \mathcal{R}$	Rooms
$k \in T$	Time steps
$l \in \mathcal{L}$	Partitions for battery degradation model
$n \in N$	Batteries
$p \in \mathcal{P}$	Partition walls of building
$s \in S$	Surfaces of building envelope

Parameters

Δt_k	Time interval between step k and step $k+1$ [h]
η^Y	Efficiency of hot-water-based heating system
$\eta_n^{ch}, \eta_n^{dch}$	Battery charging/discharging efficiency
η^R, η^T	Heat recovery system efficiency/Rated thermal efficiency of CHP unit
$\phi_{n,l}$	Piece-wise linear degradation coefficient
ψ^{HP_c}	HP cooling efficiency reduction coefficient
ψ^{HP_h}	HP heating efficiency reduction coefficient
σ_i^s	Shadowing coefficient of building surface s
τ_i^s	Transmission coefficient of windows
Vol_i	Volume for room i [m^3]
$\theta^{HP_c out}$	Cooling HP outlet temperature [K]
$\theta^{HP_h out}$	Heating HP outlet temperature [K]
θ^{gr}	Ground temperature [K]
θ_k^{ext}	Ambient temperature [K]
ξ_i^s	Amount of windows on building surface s
a	Linear term of CHP cost function [$/kWh]
A^{CWT}	External surface of cold-water tank [m^2]
A^{HWT}	External surface of hot-water tank [m^2]
A_i^f, A_i^s	Area of building floor/surface [m^2]
A_{ij}^p	Area of partition wall between room i and j [m^2]
b	Constant term of CHP cost function [$/h]
c_k^{gp}	Cost of electricity from the grid [$/kWh]
C^{sup}, C^{sdn}	Start-up/shut-down cost of CHP unit [$]
c_θ^{PCM}, c^w	PCM/water specific heat [kJ/(kg K)]
C_i^{in}	Thermal capacity of room i [kJ/K]
d	Linear term of heat transfer function [kW/K]
e	Constant term of heat transfer function [kW]
$h^{F,fuel}$	Heating value of fuel of CHP unit [kWh/fuel unit]
$I_{i,k}$	Solar irradiation [kW/m^2]
k^{PCM}	Specific heat - PCM to cold-water tank [kJ/(kg K)]
m^{PCM}	Mass of PCM [kg]
m^{CWT}	Mass of water in cold-water tank [kg]
m^{HWT}	Mass of water in hot-water tank [kg]
P_k^d, P_k^{EV}	Active power building/EV demand [kW]
P_k^{PV}	PV plant output [kW]
R^{up}, R^{dn}	Ramp-up/ramp-down rate of CHP unit [kW/h]
T^{up}, T^{dn}	Min-up/min-down time of CHP unit [h]
U	Thermal transmittance [kW/(m^2 K)]

Variables

$\dot{m}_k$	Cold-water mass flow rate [kg/s]
$\Phi_{n,l,k}$	Piece-wise linear degradation function
$\theta_{i,k}^{in}$	Indoor temperature in room i [K]
$\theta_k^{CWT}, \theta_k^{HWT}$	Temperature in cold/hot-water tank [K]
θ_k^{PCM}	Temperature in PCM [K]
G_k^{on}, G_k^{off}	ON/OFF time of CHP unit [h]
P_k^{gp}	Active power from electric grid [kW]
P_k^{CHP}	Active power from CHP unit [kW]
$P_k^{HP_c}, P_k^{HP_h}$	Cooling/heating HP thermal power [kW]
$P_{n,l,k}^{ch}, P_{n,l,k}^{dch}$	Battery charging/discharging power [kW]
$Q_{i,k}^{PCM}$	Heat transfer between the living area and the PCM [kW]
$Q_{i,k}^{env}$	Heat transfer through building envelope [kW]
$Q_{i,k}^{gr}$	Heat transfer with the ground [kW]
$Q_{i,k}^{ig}$	Internal heat gains [kW]
$Q_{i,k}^{sun}$	Thermal solar power through windows [kW]
$Q_{i,k}^{vent}$	Heat transfer due to ventilation [kW]
Q_k^{CHP}	Useful thermal power from CHP unit [kW]
Q_k^{CWTL}	Losses of cold-water tank [kW]
Q_k^{CWT}	Heat transfer between the PCM and the cold-water tank [kW]
$Q_k^{HP_c}, Q_k^{HP_h}$	Cooling/heating HP thermal power [kW]
Q_k^{HWTL}	Losses of hot-water tank [kW]
Q_k^{HWTout}	Thermal power output of hot-water tank [kW]
Q_k^{trf}	Thermal power transferred between rooms [kW]
Q_k^Y	Thermal power of the water-based heating system [kW]
$SOC_{n,l,k}$	Battery State of Charge (SOC) [kWh]
u_k, v_k	Start-up/shut-sown decision of CHP unit
w_k	ON/OFF state of CHP unit (1 = ON)
$y_{n,l,k}$	Battery charge/discharge decision (1 = charge, 0 = discharge)
z	EMS objective function [$]

(PSC) strategy is proposed that considers thermal satisfaction, available thermal storage, and energy prices to determine the dispatch of a single Heat Pump (HP) in a building MG using a multi-room building model.

In addition to the integration of clean-energy MGs, and given that the building sector is a major energy consumer and a significant contributor to Green-House Gas (GHG) emissions in today's economy, the implementation of more energy-efficient buildings is paramount. Thus,

the integration of Phase-Change Materials (PCMs) in the thermal management of buildings has received considerable attention. Numerous studies have demonstrated the benefits of incorporating PCMs into building envelopes to enhance the thermal storage capacities and insulation of walls, and thus reduce energy demand [18–24]. The authors in [25] discuss the combined operation of a radiator heating device and a PCM wallboard system to maintain indoor comfort using a Model Predictive Control (MPC) approach. Also, in [26], the thermal performance of a PCM-based Thermal Energy Storage (TES) system using an Air Conditioner (AC) to supply cooling is studied, and [27] explores the use of a PCM-embedded wall supplied by a solar collector integrated with a TES tank. However, these studies do not consider the PCM as the primary mechanism for indoor temperature control. This aspect is addressed in [28], which proposes a novel TES system using a PCM system supplied by an HP to provide cooling to a building in a two-stage thermoelectric energy management strategy. However, the study models the building as a single structure limiting the ability to account for heat exchange between rooms. Moreover, relevant thermal contribution sources such as internal heat gains, or solar radiation are not considered. In most of the existing literature, there is a predominant focus on conventional Heating, Ventilation, and Air Conditioning (HVAC) systems for temperature control within TE-MG EMS. Furthermore, although extensive research has been dedicated to PCM applications in buildings, studies that focus on PCM as the primary means for the provision of thermal power and indoor temperature control, as part of an MG, are limited.

This paper proposes a comprehensive EMS for a TE-MG capable of determining the optimal dispatch of its resources while ensuring occupants' comfort through predefined temperature settings, including the modeling of a PCM-based thermal system. The proposed model allows for properly representing the PCM energy storage capacity, considering its active cooling operation through the control of the cold-water mass flow rate, as well as its passive mode of operation when heating is provided by a water-based radiator system. Furthermore, a detailed thermal model for buildings to account for heat exchange between rooms and all relevant thermal contribution sources is included along with the representation of BESS degradation considering the Depth of Discharge (DOD) of the battery. Hence, the main contributions of the paper are as follows:

- Proposing a comprehensive EMS for a model of a PCM-based TE-MG including DERs, such as Solar Photo-Voltaic (PV) generation and BESS, and Electric Vehicle (EV) charging,
- Developing a PCM-based thermal system model that can operate in both active and passive modes to optimize thermal comfort considering the microgrid thermal power requirements and indoor temperature control,
- Demonstrating the application of the proposed EMS model to the MG of the Energy Smart Home Lab (ESHL), situated at the Karlsruhe Institute of Technology (KIT), Germany, to illustrate the components response to different price signals, with a focus on the operation of the PCM thermal system.

The rest of the paper is organized as follows: Section 2 provides a background overview of the concepts related to microgrid EMS based on an MPC approach to address uncertainties, the modeling of thermal systems including PCM, and battery degradation. Section 3 describes an optimization model for a TE-MG EMS, incorporating a comprehensive thermal model for buildings to account for various thermal contribution sources and heat exchanges, as well as the modeling of thermal systems that incorporate PCM for the provision of heating and cooling. Section 4 demonstrates the practical application of the EMS to the ESHL MG, considering the thermal needs of the MG for the hottest and coldest days of 2023. Finally, a summary and main conclusions of these studies are presented in Section 5.

2. Background

2.1. Microgrid energy management systems with uncertainties

The core of secondary control in MGs for both grid-connected and stand-alone operating modes is the EMS, which can be either centralized or decentralized [1]. In a centralized EMS, which is the focus of this paper, a central controller determines the dispatch of the resources to achieve the predefined objectives based on the information obtained from forecasting systems. Given the unpredictable nature of RES and demand, the EMS should consider these uncertainties to control the power exchange among MG's components, ensuring reliable and economical operation by the optimal commitment and dispatch of DERs. In this context, the MPC approach has been broadly used in practice to address uncertainties in EMS [1,2,29]. One of the principles within the MPC framework is a rolling horizon control, where at each time step k, the horizon moves forward while continuously solving a constrained optimization control problem. In this approach, the optimization problem is solved at each time step over a chosen time horizon T with forecasts of uncertain inputs, in order to calculate the set points for dispatchable DERs accounting for the expected values. The time intervals can have either uniform or non-uniform durations, providing flexibility in the computational complexity of the model [2].

2.2. Building thermal modeling

The thermodynamic aspects of loads in buildings can be accurately represented in an EMS model using the Thermal Equivalent Circuit (TEC) method, which is based on an analogy between thermal and electrical variables to represent heat transfer processes using an electrical circuit with lumped parameters [3]. The equivalent circuit can thus be solved by using electric circuit techniques to derive the differential equations that describe the thermodynamic processes. In this context, the thermal capacitance C of a material can be formulated as follows:

$$C = c\rho Vol \tag{1}$$

where, for a particular material, c represents the specific heat, ρ defines the density, and Vol represents the volume. The building thermal model shown in Fig. 1 is used to derive the thermal dynamic constraints of the EMS model. Hence, as per [2,30], a simpler first-order model can effectively capture the dynamics of the indoor air temperature and account for the main heat gains in each room i, as follows:

$$C_i^{in}\frac{d\theta_i^{in}}{dt} = Q_i^{Y} - Q_i^{PCM} - Q_{ij}^{trf} - Q_i^{env} - Q_i^{gr} + Q_i^{sun} + Q_i^{ig} \tag{2}$$

$$C_i^{in}\frac{d\theta_i^{in}}{dt} = Q_i^{Y} - Q_i^{PCM} - \sum_{j\in\mathcal{R}}\frac{\theta_i^{in}-\theta_j^{in}}{R_{ij}^{p}} - \frac{\theta_i^{in}-\theta^{ext}}{R_i^{s}} - \frac{\theta_i^{in}-\theta^{gr}}{R_i^{f}} + Q_i^{sun} + Q_i^{ig} \tag{3}$$

where C_i^{in}, which is the thermal capacitance that defines the indoor temperature dynamics in each room, depends on the thermal power contribution from the water-based heating system Q_i^{Y}; the thermal power

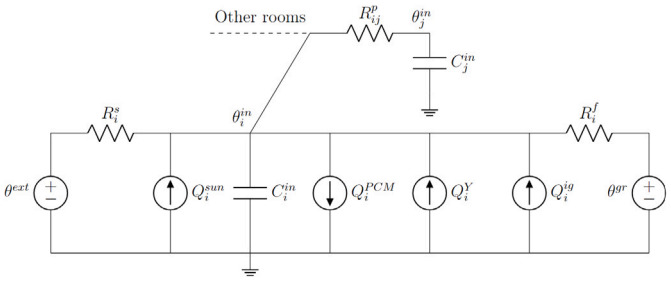

Fig. 1. Thermal circuit of a building room i.

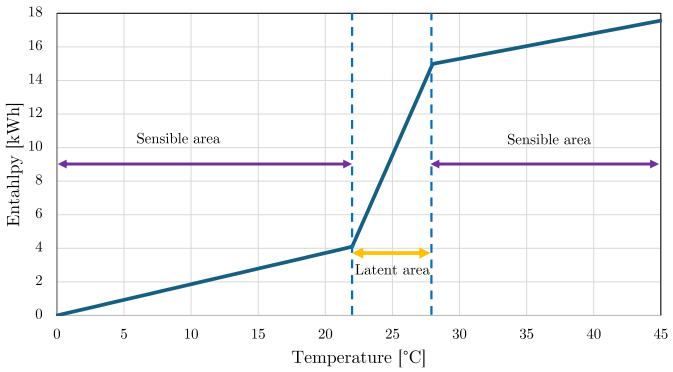

Fig. 2. Enthalpy of the PCM [31].

contribution from the PCM-based thermal system Q_i^{PCM}; the heat transfer between room i and room j Q_{ij}^{trf}; the heat transfer through the building envelope Q_i^{env}; the heat transfer between each room and the ground Q_i^{gr}; the thermal power due to solar irradiation entering through the windows Q_i^{sun}; and the internal heat gains defined for each room Q_i^{ig}. R_i^s, R_{ij}^p, and R_i^f denote the thermal resistance of the material between two adjacent areas, i.e., the outside walls, the internal walls between rooms, and the floors, respectively. Note that (2) is discretized in the EMS model using a time step on the order of minutes. All variables and parameters in these and other equations are defined in the Nomenclature section, together with their units, except for those that are dimensionless.

2.3. Phase-change material thermal systems

PCMs are a thermal storage medium based on the principle of latent heat storage. An ideal latent heat storage system does not change its temperature when thermal energy is supplied, but changes its physical state from solid to liquid to gas or vice versa [31]. Thus, given its considerably high energy density compared to sensible heat storage systems, latent heat storage systems capitalize on the enthalpy of phase change as the storage mechanism to absorb/release large amounts of heat at an almost constant temperature, as illustrated in Fig. 2. The thermodynamic equation that describes the enthalpy of PCMs is as follows [28,32]:

$$H_k^{PCM} = \int_{\theta_0^{PCM}}^{\theta_k^{PCM}} m^{PCM} c^{PCM} d\theta \tag{4}$$

where H_k^{PCM} is the enthalpy of the PCM at time k, m^{PCM} corresponds to the mass of the PCM, c^{PCM} is the specific heat of the PCM, during the phase-change process, and θ_k^{PCM} represents the PCM temperature, with θ_0^{PCM} corresponding to the starting temperature point of the phase-change process. Note that (4) must be discretized to be incorporated in the EMS formulation.

2.4. Battery degradation model

Microgrid EMS applications should consider battery degradation issues, given the impact of BESS rapid charging/discharging on battery life in the long term [29]. BESS degradation can be attributed to two factors, namely, calendar aging and cycle aging. Cycle aging is a function of the number of performed cycles and the DOD in each cycle. In this context, the Rainflow cycle-counting algorithm has proven to be an effective approach to identify the number of cycles [33]. However, given that the algorithm does not have an analytical mathematical expression, it cannot be incorporated directly within an optimization problem. Hence, [29] proposes a piece-wise linear representation for which the battery's cycle depth range is split into even partitions $l \in \mathcal{L}$, considering the range of the State of Charge (SOC) in the BESS. Assuming that only half-cycles are identified, the degradation of battery $n \in N$ can be described as follows:

$$\Phi_{n,l,k} = \frac{\phi_{n,l}}{2} \frac{\Delta t_k}{E_n} \left(P_{n,l,k}^{ch} \eta_n^{ch} + \frac{P_{n,l,k}^{dch}}{\eta_n^{dch}} \right) \tag{5}$$

$$SOC_{n,l,k+1} - SOC_{n,l,k} = \left(P_{n,l,k}^{ch} \eta_n^{ch} - \frac{P_{n,l,k}^{dch}}{\eta_n^{dch}} \right) \Delta t_k \tag{6}$$

$$\underline{SOC}_{n,l} \le SOC_{n,l,k} \le \overline{SOC}_{n,l} \tag{7}$$

$$0 \le P_{n,l,k}^{ch} \le y_{n,l,k} \bar{P}_n^{ch} \tag{8}$$

$$0 \le P_{n,l,k}^{dch} \le \left(1 - y_{n,l,k}\right) \bar{P}_n^{dch} \ \forall n \in N,\ \forall l \in \mathcal{L},\ \forall k \in T \tag{9}$$

where (5) represents the cycle aging function, (6) corresponds to the energy balance in the BESS, (7) denotes the SOC limits, and (8) and (9) model the charging and discharging power limits, respectively. The binary variable $y_{n,l,k}$ in (8) and (9) prevents the simultaneous charging/discharging of the battery. Note that each battery partition l has its own SOC, which is bounded by the partition's depth range, as per (7). The piece-wise linear degradation coefficient $\phi_{n,l}$ in (5) is obtained for each partition from the following cycle depth stress function, derived for lithium-ion batteries [29,33], which is the most widely used BESS technology in microgrid energy storage applications:

$$\Phi_\delta(\delta) = 5.23\text{x}10^{-4} \delta^{2.03} \tag{10}$$

This degradation model considers the DOD δ as the main factor for BESS degradation, neglecting temperature and average SOC due to their small impact. Furthermore, since grid-scale BESS have capacities greater than fifteen minutes, the effect of current rate on degradation is also omitted [33].

3. Energy management system for thermoelectric microgrids

The EMS model proposed here aims to optimize the operation of a TE-MG comprising a PCM-based thermal system that can operate both actively and passively, considering a detailed representation of the MG's components. For building MGs, which are grid-connected systems, the model considers power exchanges with the main grid, PV generation and BESS, and the operation of a Combined Heat and Power (CHP) unit. The heating power is assumed to be supplied by radiators through a water-based heating system powered by an HP. On the other hand, a PCM-based system supplies cooling with the support of a water tank whose temperature is maintained by another HP. The occupants' thermal comfort is addressed through the control of the indoor temperature within predefined customer-set limits.

The objective function of the EMS model proposed here aims to minimize the operating cost of the building as follows:

$$\begin{aligned} \min z = & \sum_{k \in T} \left(c_k^{gp} P_k^{gp} \Delta t_k \right) + \sum_{k \in T} \sum_{n \in N} \sum_{l \in \mathcal{L}} E_n RC_n \Phi_{n,l,k} \\ & + \sum_{k \in T} \left[\left(a P_k^{CHP} + b w_k \right) \Delta t_k + C^{sup} u_k + C^{sdn} v_k \right] \end{aligned} \tag{11}$$

where the first term pertains to the grid energy exchange prices c_k^{gp}, which are assumed to be time-dependent, as in the case of Time-of-Use (TOU) Tariffs. The second term is related to BESS degradation, where E_n represents the BESS rated energy, RC_n is the BESS replacement cost, and $\Phi_{n,l,k}$ is the piece-wise linear degradation function [29]. The third term represents the operational costs of the CHP unit, where a and b are the cost function coefficients, w_k represents ON/OFF state of the CHP unit, and u_k and v_k are the start-up/shut-down decisions, respectively, with their corresponding costs C^{sup} and C^{sdn}.

The active power balance in the MG can be represented as follows:

$$P_k^{gp} + P_k^{PV} + P_k^{CHP} + \sum_{n\in N}\sum_{l\in\mathcal{L}}\left(P_{n,l,k}^{dch} - P_{n,l,k}^{ch}\right) = P_k^{d} + P_k^{EV} + P_k^{HP_h} + P_k^{HP_c} \quad \forall k \in T \tag{12}$$

where the power from the main grid, and generation from the PV plant and the CHP unit are considered along with the charging and discharging powers of the BESS. Note that the active power consumed by both HPs, namely $P_k^{HP_h}$ and $P_k^{HP_c}$, is included here together with the demand of the household and an EV charger.

The equations describing the operation of the CHP unit are the following:

$$0 \le P_k^{CHP} \le \bar{P}^{CHP} w_k \quad \forall k \in T \tag{13}$$

$$P_k^{CHP} - P_{k-1}^{CHP} \le R^{up}\Delta t_k \quad \forall k \in T \tag{14}$$

$$P_{k-1}^{CHP} - P_k^{CHP} \le R^{dn}\Delta t_k \quad \forall k \in T \tag{15}$$

$$\left(G_{k-1}^{on} - T^{up}\right)\left(w_{k-1} - w_k\right) \ge 0 \quad \forall k \in T \tag{16}$$

$$\left(G_{k-1}^{off} - T^{dn}\right)\left(w_k - w_{k-1}\right) \ge 0 \quad \forall k \in T \tag{17}$$

$$u_k - v_k = w_k - w_{k-1} \quad \forall k \in T \tag{18}$$

$$u_k + v_k \le 1 \quad \forall k \in T \tag{19}$$

where the CHP unit constraints are represented by generation limits in (13); ramp-up (14) and ramp-down (15) constraints, which denote how fast a generator can increase or decrease the supply of active power; minimum-up (16) and minimum-down (17) constraints to account for the minimum times a generator must remain on or off; and the coordination constraints (18) and (19) that ensure the CHP generator does not start up and shut down simultaneously.

The equations that define the thermal dynamics in the MG are the following:

$$C_i^{in}\frac{\left(\theta_{i,k}^{in} - \theta_{i,k-1}^{in}\right)}{3600\Delta t_k} = Q_{i,k}^{Y} + Q_{i,k}^{sun} + Q_{i,k}^{env} - Q_{i,k}^{PCM} - Q_k^{trf} + Q_{i,k}^{ig} - Q_{i,k}^{gr} \quad \forall i \in \{LA\},\ \forall k \in T \tag{20}$$

$$C_i^{in}\frac{\left(\theta_{i,k}^{in} - \theta_{i,k-1}^{in}\right)}{3600\Delta t_k} = Q_{i,k}^{env} + Q_k^{trf} + Q_{i,k}^{ig} - Q_{i,k}^{gr} \forall i \in \{TR\},\ \forall k \in T \tag{21}$$

$$Q_k^{CHP} = \frac{h^{fuel}}{c^{fuel}}\left(aP_k^{CHP} + bw_k\right)\eta^T\eta^R \quad \forall k \in T \tag{22}$$

$$Q_k^{Y} = \eta^{Y}\left(Q_k^{HWTout} + Q_k^{CHP}\right) \quad \forall k \in T \tag{23}$$

$$Q_{i,k}^{sun} = \sum_{s\in S}\sigma_i^s I_{i,k} A_i^s \xi_i^s \tau_i^s \quad \forall i \in \{LA\},\ \forall k \in T \tag{24}$$

$$Q_{i,k}^{env} = d\left(\theta_k^{ext} - \theta_{i,k}^{in}\right) + e \quad \forall i \in \{LA\},\ \forall k \in T \tag{25}$$

$$Q_{i,k}^{env} = \sum_{s\in S} U_i^s A_i^s\left(\theta_k^{ext} - \theta_{i,k}^{in}\right) \quad \forall i \in \{TR\},\ \forall k \in T \tag{26}$$

$$Q_{i,k}^{PCM} = U^{roof} A^{PCM}\left(\theta_{i,k}^{in} - \theta_k^{PCM}\right) \quad \forall i \in \{LA\},\ \forall k \in T \tag{27}$$

$$Q_k^{trf} = U^p A^p\left(\theta_{\{LA\},k}^{in} - \theta_{\{TR\},k}^{in}\right) \quad \forall k \in T \tag{28}$$

$$Q_{i,k}^{gr} = U_i^f A_i^f\left(\theta_{i,k}^{in} - \theta^{gr}\right) \quad \forall i \in \{LA\},\{TR\},\ \forall k \in T \tag{29}$$

$$Q_{i,k}^{ig} = Np_{i,k}Q_i^p CLF_k + Q_{i,k}^{l} + Q_{i,k}^{e} \quad \forall i \in \{LA\},\{TR\},\ \forall k \in T \tag{30}$$

$$m^{HWT}c^{w}\frac{\left(\theta_k^{HWT} - \theta_{k-1}^{HWT}\right)}{3600\Delta t_k} = Q_k^{HP_h} - Q_k^{HWTout} + Q_k^{HWTL} \ \forall k \in T \tag{31}$$

$$m^{CWT}c^{w}\frac{\left(\theta_k^{CWT} - \theta_{k-1}^{CWT}\right)}{3600\Delta t_k} = Q_k^{CWT} + Q_k^{HP_c} + Q_k^{CWTL} \quad \forall k \in T \tag{32}$$

$$m^{PCM}c_{\theta}^{PCM}\frac{\left(\theta_k^{PCM} - \theta_{k-1}^{PCM}\right)}{3600\Delta t_k} = Q_k^{PCM} - Q_k^{CWT} \quad \forall k \in T \tag{33}$$

$$Q_k^{HP_h} = \psi^{HP_h}\frac{\theta^{HP_h out}}{\theta^{HP_h out} - \theta_k^{ext}}P_k^{HP_h} \quad \forall k \in T \tag{34}$$

$$Q_k^{HP_c} = \psi^{HP_c}\frac{\theta^{HP_c out}}{\theta^{HP_c out} - \theta_k^{ext}}P_k^{HP_c} \quad \forall k \in T \tag{35}$$

$$Q_k^{CWT} = k^{PCM}\dot{m}_k\left(\theta_k^{PCM} - \theta_k^{CWT}\right) \quad \forall k \in T \tag{36}$$

$$Q_k^{HWTL} = U^{HWT}A^{HWT}\left(\theta_{i,k}^{in} - \theta_k^{HWT}\right) \quad \forall i \in \{TR\},\ \forall k \in T \tag{37}$$

$$Q_k^{CWTL} = U^{CWT}A^{CWT}\left(\theta_{i,k}^{in} - \theta_k^{CWT}\right) \quad \forall i \in \{TR\},\ \forall k \in T \tag{38}$$

where the thermal dynamics of indoor air inside a typical household building, which comprises a "living" area where the thermostat is located (e.g., a living room), and the "technical" room where most TE systems are located, are modeled by (20) and (21), respectively. Q_k^{CHP} accounts for the thermal power from the CHP unit in (22), and $Q_{i,k}^{Y}$ in (23) represents the thermal power coming from the water-based heating system, which depends on the thermal power output from the hot-water tank and the CHP unit and the efficiency of the water-based system. Eq. (24) defines the thermal power from solar irradiation, considering the shadowing coefficient, solar irradiation, number of windows, and transmission coefficient of surface s. In (25) and (26), $Q_{i,k}^{env}$ represents the heat transfer through the building envelope in the living area and the technical room, respectively. The heat transfer between the living area and the PCM system through the ceiling is represented in (27) by $Q_{i,k}^{PCM}$. The heat transfer between the living area and the technical room and between each room and the ground is modeled in (28) and (29), respectively, assuming that the ground temperature remains constant throughout the day.

In (30), $Q_{i,k}^{ig}$ represents the internal heat gains from house occupants, considering a time-varying cooling factor CLF_k, as well as the heat from lighting and electric equipment. Eqs. (31) to (33) describe the thermal dynamics inside the storage systems, namely, hot-water tank, cold-water tank, and PCM, respectively. Note that to represent the variation in the PCM heat capacity as the temperature changes, the parameter c_{θ}^{PCM} in (33) is assumed to discretely change depending on the operating temperature range of the PCM system, based on a piecewise linear approximation of its non-linearly varying storage capacity. Furthermore, observe that the PCM SOC is implicitly captured through the amount of thermal energy stored, which is limited by the system mass, as sensible and latent heat relative to the PCM capacity and its temperatures. The thermal power supplied by both HPs for heating and cooling, i.e., $Q_k^{HP_h}$ and $Q_k^{HP_c}$, is modeled in (34) and (35), respectively, with their corresponding Coefficients of Performance (COP), which depend on the temperature of the HP outlet, the outside temperature, and the coefficient reduction ψ that represents the deviation from ideal efficiency and can range between 10 % and 70 % [34]. In (36), Q_k^{CWT} represents the heat exchange between the PCM system and the cold-water tank through a piping system, where $\dot{m}_k$ represents the controlled water mass flow rate, making the optimization model a Mixed Integer Nonlinear Programming (MINLP) problem. Finally, the thermal losses for the hot and cold-water tanks, i.e., Q_k^{HWTL} and Q_k^{CWTL}, are represented in (37)

and (38), respectively, with θ representing the temperatures in the various MG components.

The operational limits can be represented as follows:

$$\underline{\theta}^{HWT} \leq \theta_k^{HWT} \leq \bar{\theta}^{HWT} \quad \forall k \in T \tag{39}$$

$$\underline{\theta}^{CWT} \leq \theta_k^{CWT} \leq \bar{\theta}^{CWT} \quad \forall k \in T \tag{40}$$

$$\underline{\theta}_i^{in} \leq \theta_{i,k}^{in} \leq \bar{\theta}_i^{in} \quad \forall i \in \{LA\},\ \forall k \in T \tag{41}$$

$$0 \leq P_k^{HP_h} \leq \bar{P}^{HP_h} \quad \forall k \in T \tag{42}$$

$$0 \leq P_k^{HP_c} \leq \bar{P}^{HP_c} \quad \forall k \in T \tag{43}$$

where the temperature limits for the hot and cold-water tanks are imposed by (39) and (40), respectively; (41) models the temperature limits inside the house; and (42) and (43) limit the power consumption of both HPs.

4. Results and discussion

4.1. Description of the ESHL microgrid components

The model presented in Eqs. (5)–(9) and (11)–(38) is applied to the ESHL MG, which is a laboratory located at KIT in Germany and, as depicted in Fig. 3, is comprised of a shipping container with a 4-room 60 m^2 living area and a 20 m^2 technical room; a 4.68 kW PV system installed on the roof of the ESHL of about 36 m^2, whose power output was calculated based on solar irradiation profiles for the lab location and a typical 15 % panel efficiency; an 8 kWh BESS; a 5.5 kW CHP unit; two air-to-water HPs; two cylindrical water tanks for the storage of cold and hot water; a roof-mounted salt hydrate Delta®-Cool 24 PCM-based cooling system [35], for temperature control inside the living area of approximately 37.31 m^2, a mass of 248.16 kg, and the specific heat values for the sensible and latent regions provided in Table 1; and an 11 kW EV charging station. Furthermore, the coefficient k^{PCM} in (36) is 3.851 kJ/(kg K), as per [31].

The parameters and temperature limits for the MG's TES are presented in Table 2, as per the settings defined at the ESHL. Table 3 shows the parameters used in (24) to determine the contribution from solar thermal power. Note that ξ^s approximately corresponds to the percentage of wall surface occupied by windows, while τ^s was assumed based on typical values for standard windows. The shadowing coefficient determines the amount of sunlight that is blocked or shaded, which has been estimated based on the physical features surrounding the ESHL MG building, such as obstructions and orientation. Table 4 presents the dimensions of the ESHL MG components, while Table 5 shows the thermal transmittance that determines the heat transfer of various elements with the corresponding surrounding environment, based on [31] which defines $d = 0.10643$ and $e = 1.0805$ for (25), whereas the thermal transmittance of the technical room envelope and the hot-water tank in (26) and (37), respectively, were assumed based on typical values for similar facilities. The latter table also presents the values for the air density and air specific heat at the facility location.

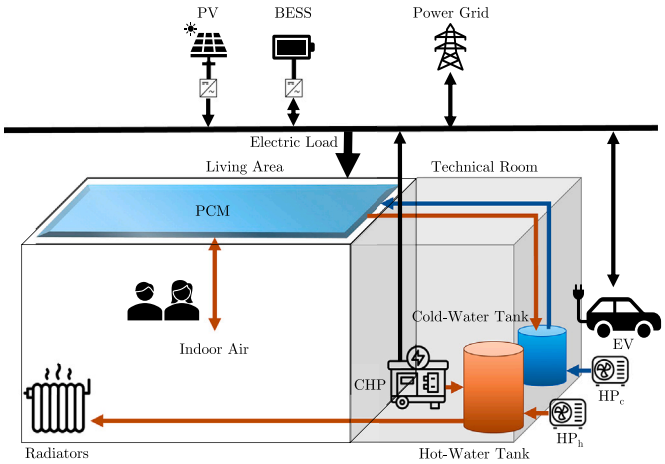

Fig. 3. ESHL MG components.

Table 1
PCM specific heat [31].

Specific heat [kJ/(kg K)]	Region	Temperature range
2.7	Solid state	$\theta^{PCM} < 22$ °C
26.33	Latent	22 °C $\leq \theta^{PCM} \leq 28$ °C
2.2	Liquid state	$\theta^{PCM} > 28$ °C

Table 2
Thermal storage systems.

Component	Capacity [kg]	Min. Temp. [°C]	Max. Temp. [°C]
Cold-water tank	200	12	13
Hot-water tank	750	55	63

Table 3
Parameters for solar contribution.

Parameter	Description	Value
τ^s	Windows transmission coefficient	0.5
σ^s	Shadowing coefficient	[0.1, 0, 0]
ξ^s	Window surface	[0.2, 0, 0.2]

Table 4
Dimensions of the MG components.

Component	Dimension
Living area	10 m x 6 m x 2.8 m
Technical room	6 m x 3.33 m x 2.8 m
Cold-water tank [31]	4.3 m^2
Hot-water tank	16.25 m^2

Table 5
Thermal parameters of the ESHL.

Component	Parameter	Value
Cold-water tank wall [31]	U^{CWT}	0.51 W/(m^2 K)
Hot-water tank wall	U^{HWT}	0.76 W/(m^2 K)
Roof [31]	U^{Roof}	12 W/(m^2 K)
Technical room envelope	U^s	0.2 W/(m^2 K)
Air specific heat	c	1.005 kJ/(kg K)
Air density	ρ	1.225 kg/m^3

The parameters for the operation of the CHP unit are presented in Table 6, based on [2], given the similarities in technology and regional characteristics, and considering the unavailability of specific data for the CHP generator at the ESHL. Furthermore, the parameters for the HPs supplying the thermal power for the heating and cooling systems are displayed in Table 7, based on [36,37]. Note that the COP is just a referential value, since the proposed formulation allows for a realistic representation of a COP that depends on the outside temperature.

4.2. Simulation results

The simulation results for the operation of the ESHL MG EMS consider the TOU Tariff proposed in [38] to analyze the behaviour of the MG's components in response to different price signals. The household

Table 6
CHP unit parameters [2].

Component	a [$/kWh]	b [$/h]	C^{sup} [$]	C^{sdn} [$]	R^{up}, R^{dn} [kW/h]	T^{up}, T^{dn} [min]	η^T	η^R
CHP Unit	0.1572	2.244	0.8438	0.2813	120	30	0.5	0.75

Table 7
HP parameters.

Component	Input power [kW]	COP	Thermal power [kW]
HP_h	1.63	4.6	7.5
HP_c	1.65	3.03	5

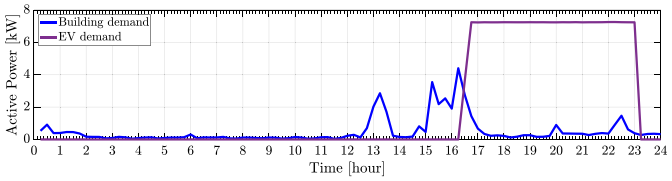

Fig. 4. Electric demand for the ESHL.

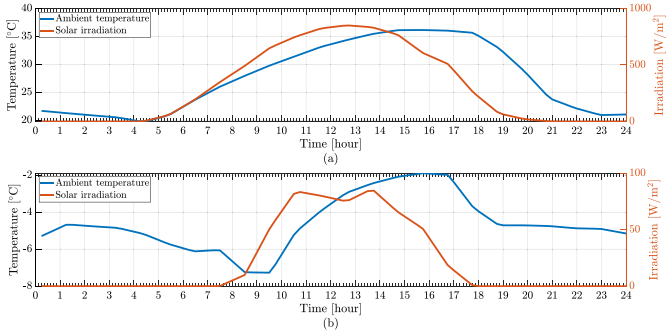

Fig. 5. Environmental conditions for the ESHL for the (a) hottest day in the summer and (b) coldest day in the winter of 2023.

electric demand was defined based on real measurements provided in [39] which are translated into internal heat gains in (30). Note that only sensible heat has been considered and that the thermal contribution from an assumed 2 occupants, presupposing typical household activities, is based on the CLF_k $\forall k$ given in [40]. Observe in Fig. 4 that a full EV charge was considered to evaluate the worst conditions in terms of power supply.

The environmental conditions considered as EMS inputs are presented in Fig. 5. Real data for the weather and solar irradiation profiles employed in the simulations were extracted from Ref. [41], for the hottest and coldest days in the region of Karlsruhe for 2023, to showcase the performance of the proposed models under boundary conditions. Note that the predefined temperature limits for the living area are assumed to be [20 °C, 25 °C], with no limits being considered for the technical room, as no temperature control mechanisms are implemented in this area. Furthermore, the starting temperature point of the phase-change process for the PCM is 22 °C. The initial BESS SOC is assumed to be 50 %, as an average starting point, i.e., not too low nor too high, and the lower and upper limits are set to typical 20 % and 90 %, respectively, with a charging/discharging efficiency of 95 %, as per [33]. It is important to mention that the presence of bilinear constraints associated with $\dot{m}_k$ in (36) requires setting appropriate bounds to prevent the system from reaching local suboptimal solutions, which were assumed to be [0, 0.15].

Table 8
Daily costs of operation for the ESHL microgrid for the hottest day in the summer of 2023.

Scenario	Grid [$]	BESS [$]	Total [$]
Case 1	11.46	0.73	12.19
Case 2	11.33	0.31	11.64

The MPC process is based on a rolling time horizon of $T = 24$ h, divided into uniform-duration intervals of $\Delta t = 15$ min each. Thus, the optimization process starts at $k = 0$, where the forecast for the next 24 h with 15 min intervals is obtained from a data set that contains the forecast for a two-day operation. This choice of control intervals is based on typical intervals used in practice for microgrid EMS (e.g., [2,5,13]), properly balancing control accuracy with computational efficiency. While longer control intervals can reduce computational burden, these may compromise the accuracy of the solution, since future time steps are considered over larger intervals in the MPC approach. On the other hand, since the proposed EMS model could be solved in approximately 4.5 minutes, the "standard" 15 min interval allows sufficient time to solve the EMS MINLP problem. The optimization problem is thus solved, with the solution for time k defining the equipment dispatch for the corresponding time intervals from 0 to 95, i.e., for 96 intervals. A linear increase in the forecast error over time is assumed to simulate uncertainties in RES and demand, as per [42].

The EMS model was implemented in the Python programming language, using Pyomo 6.5.0. All simulations were performed using Gurobi's non-convex bilinear programming solver with a Spatial Branch & Bound algorithm and Reformulation Linearization Technique (RLT) cuts on an AMD Ryzen 7 5700 G processor, with a base speed of 3.80 GHz.

4.2.1. Summer scenario

The operational costs of the ESHL TE-MG shown in Table 8 correspond to the hottest day in summer for two cases, i.e., Case 1 without BESS degradation and Case 2 with BESS degradation, with a BESS replacement cost of 139 $/kWh, based on [43].

The active power balance in the ESHL MG obtained from the proposed EMS model for the hottest day in the summer of 2023, along with the BESS SOC without and with BESS degradation, is shown in Figs. 6 and 7, respectively. Observe that the BESS operation follows an arbitrage behaviour, i.e., the battery is charged when the price is the lowest and discharged when it is highest. Note that due to the arbitrage behaviour of the microgrid components, as shown in Fig. 7, power is sold to the main grid between 6:15 and 6:30 am, from 7:30 to 3 pm, and at 3:30 and 4 pm due to higher solar irradiation, as well as when prices are highest between 12:15 pm and 1 pm, resulting in significant economic benefits. Observe that due to the increased operational costs, the CHP unit is not dispatched.

Regarding the operation of the HVAC system, Figs. 6 and 7 show that HP_c is dispatched in response to price signals, with distinct pre-cooling operations observed at 3:15 am, from 5:15 to 6 am, and at 12 pm. This helps maintain the temperature inside the cold-water tank within the imposed limits and preserves the thermal balance in the PCM, enabling it to continue absorbing heat from the living area. Note that, in this scenario, the PCM system, along with the controlled mass flow rate, plays

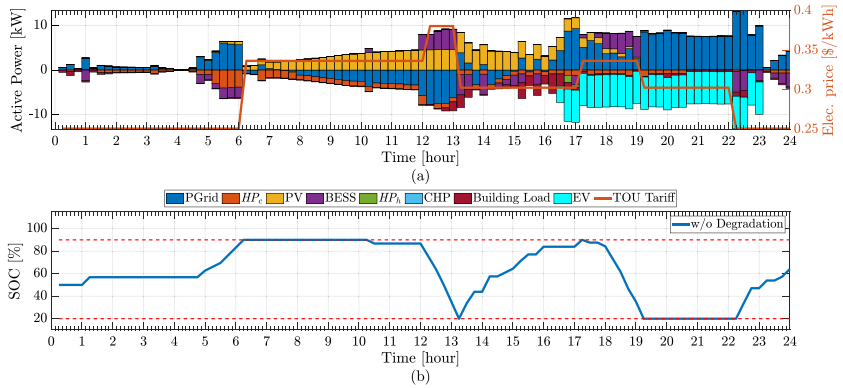

Fig. 6. (a) Power balance and (b) BESS SOC for the hottest day in the summer of 2023, without BESS degradation.

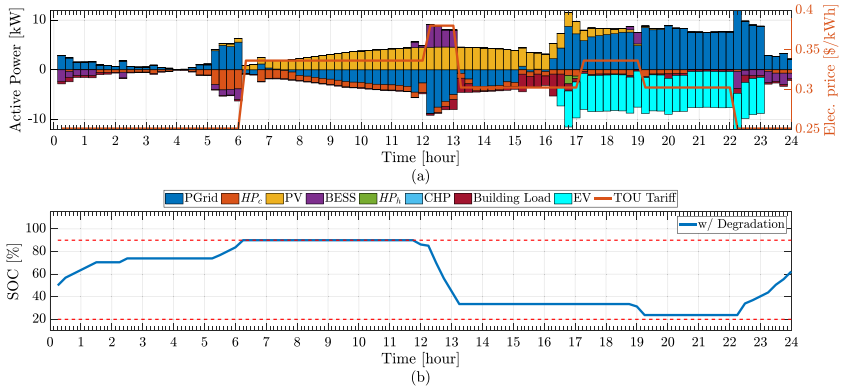

Fig. 7. (a) Power balance and (b) BESS SOC for the hottest day in the summer of 2023, with BESS degradation.

an active role in controlling the indoor temperature by regulating the heat exchange between the PCM and the cold-water tank.

The temperatures inside the living area and the different TES components, i.e., PCM, cold-water tank and hot-water tank are depicted in Fig. 8, for both Cases 1 and 2. Observe that the temperature in the PCM responds to the cold-water mass flow rate $\dot{m}_k$ which allows control of the temperature in the 4-room living area. Furthermore, note that the temperature inside the various microgrid components is maintained within the predefined limits due to the operation of the water-based thermal systems, and that the pre-cooling operations described for HP_c are reflected in the temperature inside the cold-water tank. Regarding the hot-water tank operation, observe that the temperature decreases due to the thermal losses in the technical room, while the HP maintains the temperature above the lower limit with pre-heating operations at 4:45 and 5 pm, before the price increases at 5:15 pm.

Finally, Fig. 9 illustrates the thermal balance in the PCM operating in active mode, where a significant contribution can be observed from 12:30 am to midnight in regulating the temperature in the living area due to the controlled mass flow rate. Thus, pre-cooling operations from the PCM system are also observed from 5:30 to 6 am, and at 12 and 5 pm, responding to the price signals as expected.

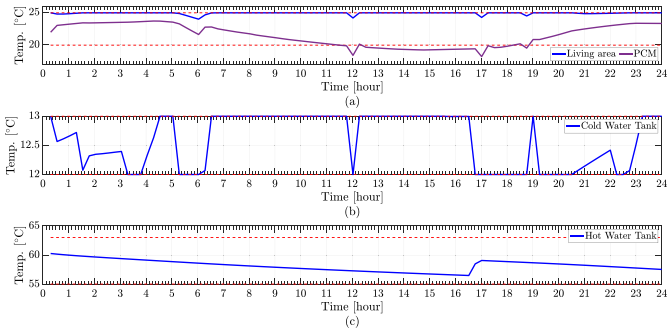

Fig. 8. Temperature in the (a) living area and PCM, (b) cold-water tank, and (c) hot-water tank for the hottest day in the summer of 2023.

4.2.2. *Winter scenario*

The operational costs of the ESHL MG for the coldest day in the winter of 2023 for the same two cases, i.e., without and with BESS degradation, are shown in Table 9. The active power balance and the BESS SOC for this coldest day are shown in Figs. 10, and 11 for the two cases considered. Compared to the summer scenario, there is a significant difference in the contribution from PV generation. Thus, note in Fig. 11 that the MG in this scenario is only capable of selling back energy to the grid at 11:45 am and from 12:15 pm to 1 pm. Moreover, as in the summer scenario, the CHP unit is not dispatched. Note also the intensive operation of HP_h to control the temperature inside the hot-water tank, with pre-heating operations occurring when the electricity price is lower, especially at 6 am. Furthermore, observe that the BESS operation is almost identical for both the summer and winter days due to the fact that the TOU Tariff is the same, which illustrates the sensitivity of the BESS to price signals. It is important to note that for winter the water flow between the PCM and the cold-water tank remains at 0 kg/s, as there is no need for cooling in the living area.

The temperatures in the MG components are shown in Fig. 12. Observe that, similar to the summer scenario, the temperature in the PCM varies in response to the changes in temperature in the living area

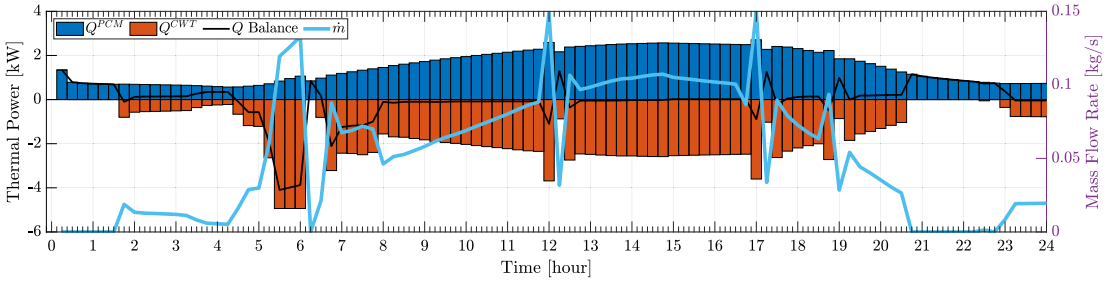

Fig. 9. PCM thermal power balance for the hottest day in the summer of 2023.

Table 9
Daily costs of operation for the ESHL microgrid for the coldest day in the winter of 2023.

Scenario	Grid [$]	BESS [$]	Total [$]
Case 1	19.69	0.71	20.40
Case 2	19.69	0.31	20.00

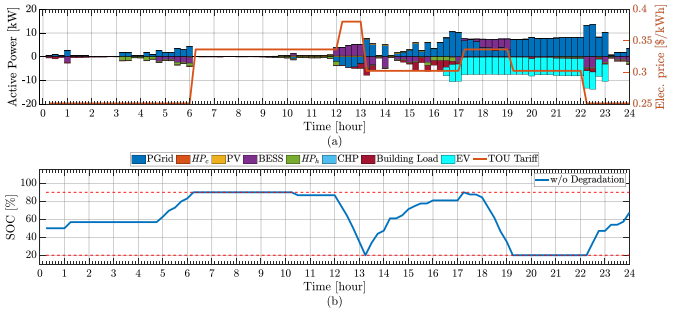

Fig. 10. (a) Power balance and (b) BESS SOC for the coldest day in the winter of 2023, without BESS degradation.

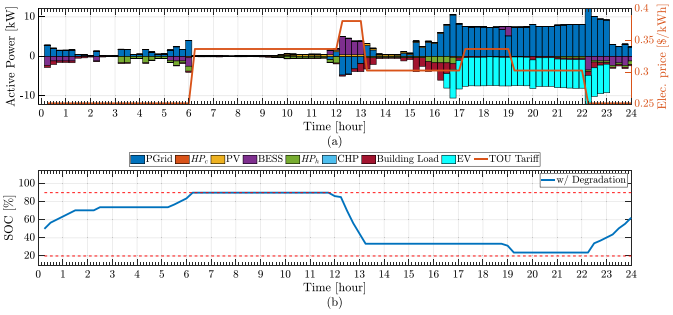

Fig. 11. (a) Power balance and (b) BESS SOC for the coldest day in the winter of 2023, with BESS degradation.

due to its thermal storage capacity, even though there is no active contribution from the PCM and the controlled mass flow rate. Note that since the temperature in the PCM is constantly below 22 °C, the storage capacity is reduced, resulting in the temperature in the PCM varying more rapidly. Furthermore, note that the temperature inside the cold and hot-water tanks is consistently maintained between the predefined limits. In contrast to the operation of the hot-water tank on the summer day, observe that the temperature inside the cold-water tank gradually increases due to the thermal losses in the technical room, with the HP operating to maintain this temperature within limits.

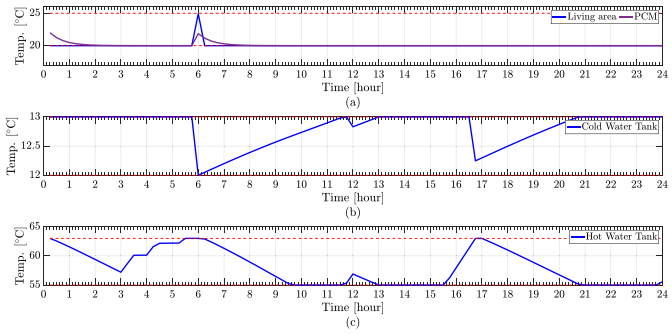

Fig. 12. Temperature in the (a) living area and PCM, (b) cold-water tank, and (c) hot-water tank for the coldest day in the winter of 2023.

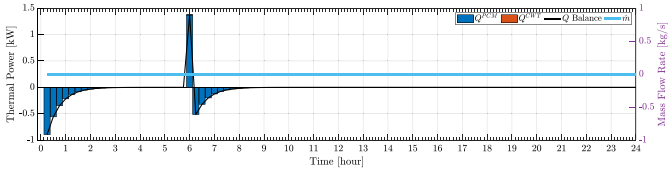

Fig. 13. PCM thermal power balance for the coldest day in the winter of 2023.

The thermal balance in the PCM is illustrated in Fig. 13 for the winter scenario. The passive contribution of the PCM acting as TES can be observed in this case, which allows for better temperature regulation in the living area through the provision of stored heat. This enables reduced costs by decreasing the operation of the HP supplying the water-based heating system.

5. Conclusions

This paper presents an MPC-based EMS model for a TE-MG, with a focus on the modeling of a PCM-based thermal system operating in both active and passive modes for indoor temperature control, and considering BESS degradation. The proposed EMS model was applied to the actual MG of the ESHL, at KIT in Germany, demonstrating the power dispatch and the temperature fluctuations of the MG's components, as well as the active/passive response of the PCM system, illustrating a cost-effective operation of the MG while meeting users' comfort requirements and power demand for the hottest and coldest days in the Karlsruhe region in 2023. Furthermore, it was shown that including BESS degradation in the model reduces the overall costs of operation, as expected.

The current operation of the ESHL equipment is based on temperature setpoints and a rule-based BESS EMS, under the existing fixed-tariff regime. The present ESHL operation was not modeled for comparison purposes, as the objective of the proposed model was to develop an

optimal operation approach for the facilities for potential future implementation, under a possible TOU regime, and comparison with the existing approach through actual measurements at the lab. Furthermore, the control of EV charging schedules through optimization could also be investigated, along with the effectiveness of the PCM-based system compared to other alternatives such as an HP-based system.

CRediT authorship contribution statement

Pablo Verdugo: Visualization, Data curation, Validation, Formal analysis, Writing – original draft, Software, Investigation, Methodology. **Claudio Cañizares:** Supervision, Writing – review & editing, Funding acquisition, Resources, Conceptualization, Project administration. **Mehrdad Pirnia:** Writing – review & editing, Resources, Supervision, Funding acquisition, Project administration, Conceptualization. **Thomas Leibfried:** Conceptualization, Resources, Writing – review & editing, Supervision.

Funding

This work has been supported by the Natural Sciences and Engineering Research Council of Canada (NSERC).

Declaration of competing interest

The authors declare that they have no known competing financial interests or personal relationships that could have appeared to influence the work reported in this paper.

Acknowledgment

We would like to thank our colleagues Felicitas Müller and Johanna Geis-Schroer at KIT, who greatly contributed to the development of the work reported in this paper with their expertise and the provision of data.

Data availability

Data will be made available upon request.

References

[1] D.E. Olivares, C.A. Canizares, M. Kazerani, A centralized Energy management system for isolated microgrids, IEEE Trans. Smart Grid 5 (4) (2014) 1864–1875.
[2] W. Violante, C.A. Cañizares, M.A. Trovato, G. Forte, An Energy management system for isolated microgrids with thermal Energy resources, IEEE Trans. Smart Grid 11 (4) (2020) 2880–2891.
[3] W. Mendieta, C.A. Cañizares, Primary frequency control in isolated microgrids using thermostatically controllable loads, IEEE Trans. Smart Grid 12 (1) (2021) 93–105.
[4] M. Abuelhamd, C.A. Cañizares, Dynamic model of integrated electricity and district heating for remote communities, Appl. Energy 376 (2024) 124337.
[5] Y. Wang, Y. Li, Y. Cao, M. Shahidehpour, L. Jiang, Y. Long, Y. Deng, W. Li, Optimal operation strategy for multi-energy microgrid participating in auxiliary service, IEEE Trans. Smart Grid 14 (5) (2023) 3523–3534.
[6] H. Masrur, M. Shafie-Khah, M.J. Hossain, T. Senjyu, Multi-energy microgrids incorporating EV integration: optimal design and resilient operation, IEEE Trans. Smart Grid 13 (5) (2022) 3508–3518.
[7] Z. Li, L. Wu, Y. Xu, S. Moazeni, Z. Tang, Multi-stage real-time operation of a multi-energy microgrid with electrical and thermal Energy Storage assets: a data-driven MPC-ADP approach, IEEE Trans. Smart Grid 13 (1) (2022) 213–226.
[8] S.E. Ahmadi, M. Marzband, A. Ikpehai, A. Abusorrah, Optimal stochastic scheduling of plug-in electric vehicles as Mobile Energy Storage Systems for resilience enhancement of multi-agent multi-energy networked microgrids, J. Energy Storage 55 (2022) 105566.
[9] Z. Li, Y. Xu, Optimal coordinated Energy dispatch of a multi-energy microgrid in Grid-connected and islanded modes, Appl. Energy 210 (2018) 974–986.
[10] L. Moretti, E. Martelli, G. Manzolini, An efficient robust optimization Model for the unit commitment and dispatch of multi-energy systems and microgrids, Appl. Energy 261 (2020) 113859.
[11] P. Emrani-Rahaghi, H. Hashemi-Dezaki, A. Ketabi, Efficient voltage control of Low voltage distribution Networks using integrated optimized Energy management of networked residential multi-energy microgrids, Appl. Energy 349 (2023) 121391.
[12] A. Anvari-Moghaddam, A. Rahimi-Kian, M.S. Mirian, J.M. Guerrero, A multi-agent based Energy management solution for integrated buildings and microgrid system, Appl. Energy 203 (2017) 41–56.
[13] G. Liu, T. Jiang, T.B. Ollis, X. Zhang, K. Tomsovic, Distributed Energy management for community microgrids considering network operational constraints and building thermal dynamics, Appl. Energy 239 (2019) 83–95.
[14] J. Vasilj, D. Jakus, P. Sarajcev, Robust nonlinear economic MPC based management of a multi Energy microgrid, IEEE Trans. Energy Convers. 36 (2) (2021) 1528–1536.
[15] C. Zhang, Y. Xu, Z. Li, Z.Y. Dong, Robustly coordinated operation of a multi-energy microgrid with flexible electric and thermal loads, IEEE Trans. Smart Grid 10 (3) (2019) 2765–2775.
[16] N.A. Efkarpidis, S.A. Vomva, G.C. Christoforidis, G.K. Papagiannis, Optimal day-to-day scheduling of multiple Energy assets in residential buildings equipped with variable-speed heat pumps, Appl. Energy 312 (2022) 118702.
[17] M. Frahm, T. Dengiz, P. Zwickel, H. Maaß, J. Matthes, V. Hagenmeyer, Occupant-oriented demand response with multi-zone thermal building control, Appl. Energy 347 (2023) 121454.
[18] H. Cui, L. Zhang, H. Yang, Y. Shi, Optimizing thermal comfort and Energy efficiency in hospitals with PCM-Enhanced wall systems, Energy. Build. 323 (2024) 114740.
[19] H. Yin, A. Norouziasas, M. Hamdy, PCM as an Energy flexibility asset: how design and operation Can Be optimized for heating in residential buildings? Energy. Build. 322 (2024) 114721.
[20] H. Al Jebaei, A. Aryal, I.K. Jeon, A. Azzam, Y.-R. Kim, J.-C. Baltazar, Evaluating the potential of optimized PCM-Wallboards for reducing Energy consumption and CO_2 emission in buildings, Energy. Build. 315 (2024) 114320.
[21] L. Ouhsaine, H. Ramenah, M. El Ganaoui, A. Mimet, Dynamic state-space Model and performance analysis for solar active walls embedded phase change material, Sustain. Energy Grids Netw. 24 (2020) 100401.
[22] W. Hu, Y. Duan, D. Li, C. Zhang, H. Yang, R. Yang, Optimizing the indoor thermal environment and daylight performance of buildings with PCM glazing, Energy. Build. 318 (2024) 114481.
[23] N. Kulumkanov, S.A. Memon, S.A. Khawaja, Evaluating future building Energy efficiency and environmental sustainability with PCM integration in building envelope, J. Build. Eng. 93 (2024) 109413.
[24] W. Zhang, Y. Shi, H. Yang, Y. Zou, X. Cao, H. Cui, Design optimization of passive PCM-Enhanced hospital buildings for efficient Energy-saving, J. Energy Storage 91 (2024) 112037.
[25] Z. Wei, J.K. Calautit, Field experiment testing of a low-cost Model Predictive Controller (MPC) for building heating systems and analysis of Phase Change Material (PCM) integration, Appl. Energy 360 (2024) 122750.
[26] V.V. Tyagi, A.K. Pandey, D. Buddhi, R. Kothari, Thermal performance assessment of encapsulated PCM based thermal management system to reduce peak Energy demand in buildings, Energy. Build. 117 (2016) 44–52.
[27] M. Hosseini, S.H. Tasnim, S. Mahmud, Application of PCM for radiant heating of residential buildings in Canada towards achieving nearly zero energy buildings, J. Energy Storage 102 (2024) 114030.
[28] F. Wei, Y. Li, Q. Sui, X. Lin, L. Chen, Z. Chen, Z. Li, A novel thermal Energy Storage system in smart building based on phase change material, IEEE Trans. Smart Grid 10 (3) (2019) 2846–2857.
[29] S. Córdova, C. Cañizares, A. Lorca, D.E. Olivares, An Energy management system with short-term fluctuation reserves and battery degradation for isolated microgrids, IEEE Trans. Smart Grid 12 (6) (2021) 4668–4680.
[30] I. Calero, C.A. Cañizares, K. Bhattacharya, R. Baldick, Duck-curve mitigation in power Grids with high penetration of PV generation, IEEE Trans. Smart Grid 13 (1) (2022) 314–329.
[31] S. Maier, Integration eines Gebäudekühlsystems mit Phasenwechselmaterial in ein Gebäudeenergiemanagementsystem, Master's thesis, Karlsruhe Institute of Technology, 2017.
[32] M. Mohiti, M. Mazidi, N. Oggioni, D. Steen, L.A. Tuan, An IGDT-Based Energy management system for local Energy communities considering phase-change thermal Energy Storage, IEEE Trans. Ind. Appl. 60 (3) (2024) 4470–4481.
[33] B. Xu, J. Zhao, T. Zheng, E. Litvinov, D.S. Kirschen, Factoring the cycle aging cost of batteries participating in electricity markets, IEEE Trans. Power Syst. 33 (2) (2018) 2248–2259.
[34] B. Aluisio, M. Dicorato, G. Forte, G. Litrico, M. Trovato, Integration of heat production and thermal comfort models in microgrid operation planning, Sustain. Energy Grids Netw. 16 (2018) 37–54.
[35] DELTA®-COOL 24, Dörken GmbH & Co. KG, https://pcmsouth.com/assets/docs/DELTA-COOL24_2007364204631.70150629.pdf (Accessed March 1, 2025).
[36] Specifications Table for EHBH-D9W / ERGA04-08DV, Daikin. [Online]. Available: https://www.daikin-ce.com/en_us/products/product.table.html/EHBH-D9W---ERGA04-08DV.html.
[37] Air to Water Outdoor Units SUZ-SWM40VA / SUZ-SWM60VA, Mitsubishi Electric. [Online]. Available: https://bailos.gr/wp-content/uploads/2021/05/Brochure-SUZ-SWM40-60-Udedel.pdf.
[38] I. Mauser, Multi-modal building Energy management, Ph.D. dissertation, Karlsruhe Institute of Technology, 2017.
[39] T. Sandmeier, Electrical Consumption Data from a Three Months Living Lab Experiment in the Energy Smart Home Lab, 2023.
[40] V. Thomas, Internal Heat Gains (IHG), https://energy-models.com/internal-heat-gains-ihg (Accessed November 10, 2024).
[41] Meteoblue, Weather Karlsruhe, https://www.meteoblue.com/en/weather/week/karlsruhe_germany_2892794 (Accessed August 11, 2024).
[42] D. Romero-Quete, C.A. Cañizares, An affine arithmetic-based Energy management system for isolated microgrids, IEEE Trans. Smart Grid 10 (3) (2019) 2989–2998.
[43] O. Catsaros, Lithium-ion battery pack prices hit record low of $139/kWh, BloombergNEF, Tech. Rep., 2023.